Frequency based coarse space for FETI method in nonlinear structural dynamic problems

Computers and Structures 325 (2026) 108207

Contents lists available at ScienceDirect

Computers and Structures

journal homepage: www.elsevier.com/locate/cas

# Frequency based coarse space for FETI method in nonlinear structural dynamic problems

Andrea Saponaro*, Giuseppe Battiato, Christian Maria Firrone, Stefano Zucca

*Department of Mechanical and Aerospace Engineering, Politecnico di Torino, Corso Duca degli Abruzzi 24, 10129, Torino, Italy*

ARTICLE INFO

*Keywords:*
Domain decomposition
FETI
HBM
Nonlinear dynamics
HPC
Linear systems
GMRES

ABSTRACT

The nonlinear structural dynamic analysis of mechanical assemblies with nonlinearities poses significant computational challenges, especially as the size and complexity of the Finite Element model increases. This is especially true in turbomachinery, where the large Finite Element models of bladed-disk assemblies often require the use of reduced order models to reduce computational cost. However, reduced order models rely on physical assumptions and involve additional solution steps, which may not always be computationally efficient or feasible.

To address these challenges, domain decomposition methods offer a promising alternative. They constitute a robust and well-established class of techniques for tackling large-scale problems in the context of High Performance Computing. Among the various domain decomposition strategies, the Finite Element Tearing and Interconnecting (FETI) method is widely recognized for its robustness and efficiency in engineering applications. When applied to nonlinear dynamic problems with localized nonlinearities in the frequency domain, the FETI formulation leads to an indefinite, non-symmetric linear system. Such a system is typically solved iteratively using the GMRES algorithm, whose convergence can be significantly accelerated by introducing coarse spaces.

In the FETI framework, state-of-the-art coarse spaces for the solution of static and dynamic problems are typically constructed using the rigid body modes of the individual domains resulting from the Finite Element model decomposition. While this approach performs well for static and time domain dynamic analyses, it loses its effectiveness when applied to frequency domain solutions. This paper introduces a novel coarse space, referred to as the Frequency Based Coarse Space, specifically designed for the solution of nonlinear structural dynamic problems in the frequency domain.

## 1. Introduction

One of the key aspects in the design of bladed disks in turbomachinery is the need to reduce blade vibration amplitudes in order to prevent structural failures caused by High Cycle Fatigue (HCF) [1]. To this end, accurately predicting the vibration amplitude of blades in the presence of contact nonlinearities at mechanical joint interfaces, under actual operating conditions, is essential. One of the most widely adopted approaches for computing the nonlinear forced response of such components combines contact elements with the Harmonic Balance Method (HBM) [2]. This formulation enables an efficient analysis of nonlinear dynamic systems by solving the governing equations directly in the frequency domain. As a result, the computational cost is significantly reduced compared to time domain simulations, while still accurately capturing key nonlinear phenomena such as contact interactions and friction damping at the interfaces. Although a reduction in computational cost is achieved, the continuous increase in Finite Element (FE) model size still poses a significant computational challenge. Reduced-Order Models (ROMs) are therefore introduced to reduce the size of the FE model [3–9]. While ROMs represent a well-established class of methods, they rely on physical assumptions and, in order to be useful for the mechanical design of components, require a reduction and subsequent expansion process that is not always practical or computationally feasible.

Nowadays, the increasing computational power of High Performance Computing (HPC) infrastructures plays a crucial role in enabling the dynamic analysis of large-scale FE models exhibiting nonlinear behavior in operation, such as bladed disks with frictional contacts. In this context, domain decomposition methods represent a robust and well-established

* Corresponding author.
*Email addresses:* andrea.saponaro@polito.it (A. Saponaro), giuseppe.battiato@polito.it (G. Battiato), christian.firrone@polito.it (C.M. Firrone), stefano.zucca@polito.it (S. Zucca).

https://doi.org/10.1016/j.compstruc.2026.108207
Received 6 October 2025; Accepted 19 March 2026
Available online 28 March 2026

class of techniques that seamlessly integrate engineering modeling, numerical methods, and parallel computing [10].

Domain decomposition methods can be broadly classified into two main categories: overlapping and non-overlapping methods. Among the non-overlapping methods the Finite Element Tearing and Interconnecting (FETI) method is known for its robustness and efficiency in the field of engineering problems [11]. Since its introduction in 1991, several variants [12–16] and applications have been proposed for the solution of wave propagation problems [17] as well as structural problems [18–20]. In the field of structural problems, the FETI method has been applied to the solution of nonlinear structural problems including geometric nonlinearities [20,21] and friction/frictionless contact problems. Focusing on nonlinear dynamic problems both in the time domain and in the frequency domain some applications can be found in [20,22].

When the FETI method is applied to nonlinear dynamic problems in combination with the HBM, the introduction of Lagrange multipliers leads to an interface problem expressed as a linear system. This system is typically solved using the GMRES algorithm, owing to the non-symmetric and indefinite nature of the matrices involved. To improve convergence, various strategies have been proposed, including preconditioning techniques [23] and deflation methods [24,25]. The latter approach relies on constructing coarse spaces that project the interface problem onto a more favorable subspace, thereby accelerating GMRES convergence. Identifying effective coarse spaces remains a key challenge, particularly for indefinite systems.

One of the most commonly adopted coarse spaces for solving linear and nonlinear dynamic problems is based on the rigid body modes of the unconstrained domains [18,20,22], which span the null space of the corresponding stiffness matrices. While this approach is effective for time domain problems [18], it may result in slow GMRES convergence or even stagnation when applied to frequency domain problems. The goal of this paper is to introduce a novel coarse space, referred to as the Frequency Based Coarse Space (FBCS), designed to be suitable for parallel computing and to significantly accelerate GMRES convergence while mitigating the adverse effects introduced by domain decomposition and by the frequency range under analysis.

This paper is organized as follows: the methodology section first describes how the FETI method is applied to nonlinear dynamic problems with localized nonlinearities, followed by the formulation of the resulting interface problem and an overview of deflation techniques. Next, the conventional rigid body coarse space (RBCS) and the newly proposed FBCS are presented. Since parallel implementation and domain decomposition play a key role in solver efficiency, a dedicated section discusses implementation aspects. Finally, the results section provides a scalability analysis, examines the influence of frequency range on GMRES convergence, and demonstrates the effectiveness and robustness of the proposed FBCS through a validation study on a full bladed-disk assembly.

The main contribution of this work is the introduction of a novel coarse space, the FBCS, specifically designed for frequency domain nonlinear dynamic analyses. This new approach is suitable for parallel computing and significantly accelerates GMRES convergence, mitigating the negative effects introduced by domain decomposition and by the frequency range under investigation.

## 2. Methodology

This section provides a brief overview of the application of the FETI method to the solution of nonlinear dynamic problems involving localized nonlinearities in the frequency domain [11]. The resulting linear interface problem arising from the FETI method is analyzed with a focus on its properties and on its iterative solution using the GMRES method [26]. Due to the spectral properties of the matrices involved in the interface problem, a projection-based preconditioner (known as deflation) is introduced to accelerate GMRES convergence [24]. A commonly used coarse space based on the rigid body modes of the unconstrained domain is examined, and its advantages and disadvantages are discussed [18,20,22]. Finally, the new FBCS is introduced as a means to further improve GMRES convergence. For both coarse spaces, explanations from both mathematical and physical perspectives are provided.

### 2.1. FETI method and HBM

We consider a mechanical assembly with localized nonlinearities occupying a bounded domain $\Omega \subset \mathbb{R}^3$ with boundary $\partial\Omega = \Gamma_D \cup \Gamma_N$. Let $x(\mathbf{x}, t)$ denote the displacement field at position $\mathbf{x}$ and time $t$. The elasticity problem is formulated as:

$$\rho(\mathbf{x})\ddot{\mathbf{x}}(\mathbf{x}, t) - \nabla \cdot \sigma\left(x(\mathbf{x}, t)\right) = \boldsymbol{f}(\mathbf{x}, t) - \boldsymbol{f}_{nl}\left(x(\mathbf{x}, t), \dot{x}(\mathbf{x}, t)\right) \text{ with } \mathbf{x} \in \Omega. \tag{1}$$

$\rho(\mathbf{x})$ is the material density, $\sigma(x)$ is stress tensor from the constitutive law, $\boldsymbol{f}(\mathbf{x}, t)$ denotes external forces, and $\boldsymbol{f}_{nl}\left(x(\mathbf{x}, t), \dot{x}(\mathbf{x}, t)\right)$ represents the nonlinear forces due to contacts in the assembly. The boundary conditions are:

$$\begin{aligned} &x(\mathbf{x}, t) = 0 \text{ on } \Gamma_D, \\ &\sigma(x(\mathbf{x}, t))\,\mathbf{n} = g(\mathbf{x}, t) \text{ on } \Gamma_N, \end{aligned} \tag{2}$$

where $\mathbf{n}$ is the outward unit normal and $g(\mathbf{x}, t)$ is the prescribed traction on $\Gamma_N$. The weak form is obtained and discretized using the Finite Element method. Assembly over all elements yields the semi-discrete system representing the time domain equation of motion (EQM):

$$\boldsymbol{M}\ddot{\boldsymbol{x}} + \boldsymbol{C}\dot{\boldsymbol{x}} + \boldsymbol{K}\boldsymbol{x} = \boldsymbol{f} - \boldsymbol{f}_{nl}(\boldsymbol{x}, \dot{\boldsymbol{x}}), \tag{3}$$

where $\boldsymbol{M}$, $\boldsymbol{C}$ and $\boldsymbol{K} \in \mathbb{R}^{n \times n}$ (with $n$ being the number of degrees of freedom) are the FE mass, the linearized damping and the stiffness matrix, respectively. $\boldsymbol{x} \in \mathbb{R}^n$ is the vector of the FE nodal displacements and $\boldsymbol{f}$ and $\boldsymbol{f}_{nl}(\boldsymbol{x}, \dot{\boldsymbol{x}}) \in \mathbb{R}^n$ are the vectors of the external excitation and the nonlinear contact forces, respectively.

Since we are interested in the steady-state periodic response, assuming the external excitation $\boldsymbol{f}$ to be periodic the system is not integrated in time. Instead, the HBM is applied by expressing the nodal displacements as a truncated Fourier series [2]:

$$[-\omega^2 \boldsymbol{M} + i\omega \boldsymbol{C} + \boldsymbol{K}]\tilde{\boldsymbol{x}}_c - \tilde{\boldsymbol{f}}_c + \tilde{\boldsymbol{f}}_{c,nl}(\tilde{\boldsymbol{x}}_c) = \boldsymbol{o}, \tag{4}$$

where $\tilde{\boldsymbol{x}}_c \in \mathbb{C}^n$ is the vector of the first order Fourier coefficients of the nodal displacements, $\tilde{\boldsymbol{f}}_c$ and $\tilde{\boldsymbol{f}}_{c,nl}(\tilde{\boldsymbol{x}}_c) \in \mathbb{C}^n$ are the first order Fourier coefficients of the external excitation and the nonlinear contact forces, respectively and $\boldsymbol{o}$ is the zero vector. The subscript $c$ refers to complex terms. This formulation fully defines the mathematical problem, including the governing PDE, the spatial domain and boundary conditions, the FE spatial discretization, the nonlinearities present in the assembly, and the frequency-domain method used to compute the periodic steady-state response. (4) is solved in real algebra, leading to:

$$\boldsymbol{D}(\omega)\tilde{\boldsymbol{x}} - \tilde{\boldsymbol{f}} + \tilde{\boldsymbol{f}}_{nl}(\tilde{\boldsymbol{x}}) = \boldsymbol{o} \text{ with } \boldsymbol{D}(\omega) = \begin{bmatrix} -\omega^2 \boldsymbol{M} + \boldsymbol{K} & -\omega \boldsymbol{C} \\ \omega \boldsymbol{C} & -\omega^2 \boldsymbol{M} + \boldsymbol{K} \end{bmatrix}, \tag{5}$$

where $\tilde{\boldsymbol{x}}$, $\tilde{\boldsymbol{f}}$, $\tilde{\boldsymbol{f}}_{nl}(\tilde{\boldsymbol{x}}) \in \mathbb{R}^{2n}$ and $\boldsymbol{D}(\omega) \in \mathbb{R}^{2n \times 2n}$ is the dynamic stiffness matrix, having a quadratic dependence on the frequency $\omega$.

The main idea of domain decomposition (DD) methods is to split a large FE domain into smaller domains to simplify the solution process. Many computations are local, but global operations (such as interface or coarse-space solves) are generally needed for consistency and convergence. DD techniques can be applied in parallel, yet they also offer algorithmic benefits in serial computations, including improved conditioning and solver modularity [10]. As an example, Fig. 1 shows, on the left, the FE model of two bodies interacting through a contact interface, and, on the right, how the domain decomposition is performed to make the problem suitable for solution using parallel computing in an HPC environment.

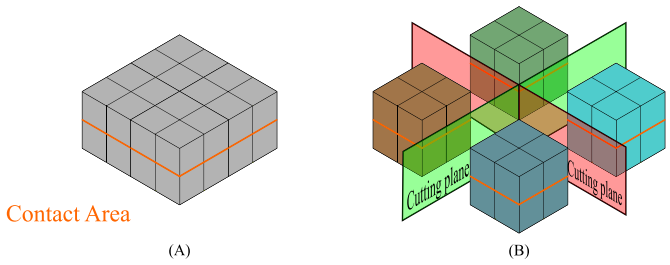


**Fig. 1.** FE model of two bodies in contact (A), and decomposition (B).

The FETI method applied to an FE model decomposed in $N$ domains leads to the following system of nonlinear algebraic equations:

$$\begin{cases} \boldsymbol{D}_s(\omega)\tilde{\boldsymbol{x}}_s - \tilde{\boldsymbol{f}}_s + \tilde{\boldsymbol{f}}_{nl,s}(\tilde{\boldsymbol{x}}_s) + \boldsymbol{B}_s^T\tilde{\lambda} = \boldsymbol{o} \quad \forall s = 1 \dots N, \\ \sum_{s=1}^{N} \boldsymbol{B}_s\tilde{\boldsymbol{x}}_s = \boldsymbol{o}, \end{cases} \tag{6}$$

where the subscript $s$ denotes the $s^{\text{th}}$ FE domain resulting from the decomposition. In (6), $\boldsymbol{B}_s \in \mathbb{R}^{m\times 2n_s}$ (with $m$ the number of Lagrange multipliers) is the Boolean connectivity matrix built using a non-redundant scheme. The vector $\tilde{\lambda} \in \mathbb{R}^m$ contains the forces exchanged between domains and can be interpreted as the Lagrange multipliers associated with the constraints represented by the second equation in (6). To clarify the role of the Lagrange multipliers $\tilde{\lambda}$ and the contact forces $\tilde{\boldsymbol{f}}_{nl,s}(\tilde{\boldsymbol{x}}_s)$ in the equilibrium of the single domain, Fig. 2 provides a detailed view of a generic domain $\Omega_s$ including a contact interface. It is important to notice that the nonlinearity in (6) is only given by the term $\tilde{\boldsymbol{f}}_{nl,s}(\tilde{\boldsymbol{x}}_s)$. All the other terms including the interface problem are entirely linear.

The proposed methodology can be applied to mechanical assemblies with localized contact nonlinearities. The decomposition process is performed to avoid cutting planes that are coincident with the contact areas. This means that it is not necessary for a contact area to belong fully to a single domain. Considering the contact model discussed in Section 3.2, the hypothesis of avoiding cutting planes coincident with the contact area makes the interface problem linear. As a remark, it's important to clarify that having an interface belonging to a single domain does not mean the contact interface belongs entirely to that domain; further details can be found in [22].

The nonlinear system (6) can be solved for the nonlinear displacements $\tilde{\boldsymbol{x}}_s$ and $\tilde{\lambda}$ using an iterative solution method, such as the Newton-Raphson (NR) method. At the $k^{th}$ iteration of NR, the linearization of (6) can be viewed in a three step process:

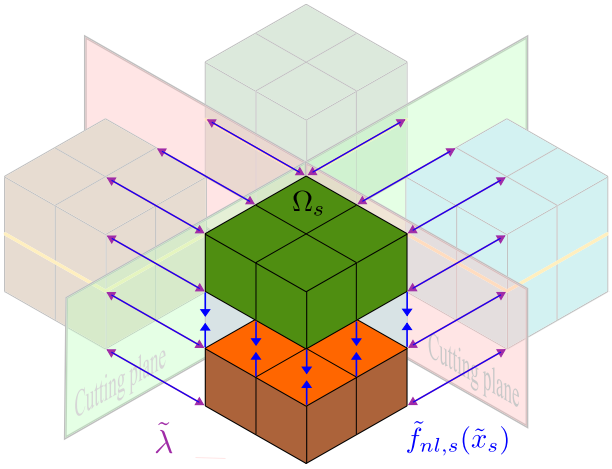


**Fig. 2.** Focus on Lagrange multipliers and contact forces.

1. Definition of the residuals $\boldsymbol{r}_{L,s}(\tilde{\boldsymbol{x}}_s^k, \tilde{\lambda}^k)$ and $\boldsymbol{r}_B(\tilde{\boldsymbol{x}}_{1\dots N}^k, \tilde{\lambda}^k)$:

$$\begin{cases} \boldsymbol{r}_{L,s}(\tilde{\boldsymbol{x}}_s^k, \tilde{\lambda}^k) = \boldsymbol{D}_s(\omega)\tilde{\boldsymbol{x}}_s^k - \tilde{\boldsymbol{f}}_s + \tilde{\boldsymbol{f}}_{nl,s}(\tilde{\boldsymbol{x}}^k) + \boldsymbol{B}_s^T\tilde{\lambda}^k \ \forall s = 1 \dots N, \\ \boldsymbol{r}_B(\tilde{\boldsymbol{x}}_{1\dots N}^k, \tilde{\lambda}^k) = \sum_{s=1}^{N} \boldsymbol{B}_s\tilde{\boldsymbol{x}}_s^k. \end{cases} \tag{7}$$

2. Application of the NR to the displacement fields $\tilde{\boldsymbol{x}}_s^k$ and the Lagrange multipliers vector $\tilde{\lambda}$:

$$\begin{cases} \frac{\partial \boldsymbol{r}_{L,s}(\tilde{\boldsymbol{x}}_s^k, \tilde{\lambda}^k)}{\partial \tilde{\boldsymbol{x}}_s^k}\Delta\tilde{\boldsymbol{x}}_s^k + \frac{\partial \boldsymbol{r}_{L,s}(\tilde{\boldsymbol{x}}_s^k, \tilde{\lambda}^k)}{\partial \tilde{\lambda}^k}\Delta\tilde{\lambda}^k = -\boldsymbol{r}_{L,s}(\tilde{\boldsymbol{x}}_s^k, \tilde{\lambda}^k) \ \forall s = 1 \dots N, \\ \frac{\partial \boldsymbol{r}_B(\tilde{\boldsymbol{x}}_{1\dots N}^k, \tilde{\lambda}^k)}{\partial \tilde{\boldsymbol{x}}_{1\dots N}^k}\Delta\tilde{\boldsymbol{x}}_s^k + \frac{\partial \boldsymbol{r}_B(\tilde{\boldsymbol{x}}_{1\dots N}^k, \tilde{\lambda}^k)}{\partial \tilde{\lambda}^k}\Delta\tilde{\lambda}^k = -\boldsymbol{r}_B(\tilde{\boldsymbol{x}}_{1\dots N}^k, \tilde{\lambda}^k). \end{cases} \tag{8}$$

The residuals $\boldsymbol{r}_{L,s}(\tilde{\boldsymbol{x}}_s^k, \tilde{\lambda}^k)$ and $\boldsymbol{r}_B(\tilde{\boldsymbol{x}}_{1\dots N}^k, \tilde{\lambda}^k)$ are differentiable and their partial derivatives leads to:

$$\begin{aligned} &\frac{\partial \boldsymbol{r}_{L,s}(\tilde{\boldsymbol{x}}_s^k, \tilde{\lambda}^k)}{\partial \tilde{\boldsymbol{x}}_s^k} = [\boldsymbol{D}_s(\omega) + \nabla\tilde{\boldsymbol{f}}_{nl}(\tilde{\boldsymbol{x}}_s^k)], \ \frac{\partial \boldsymbol{r}_{L,s}(\tilde{\boldsymbol{x}}_s^k, \tilde{\lambda}^k)}{\partial \tilde{\lambda}^k} = \boldsymbol{B}_s^T, \\ &\frac{\partial \boldsymbol{r}_B(\tilde{\boldsymbol{x}}_{1\dots N}^k, \tilde{\lambda}^k)}{\partial \tilde{\boldsymbol{x}}_{1\dots N}^k} = \boldsymbol{B}_s, \ \frac{\partial \boldsymbol{r}_B(\tilde{\boldsymbol{x}}_{1\dots N}^k, \tilde{\lambda}^k)}{\partial \tilde{\lambda}^k} = \boldsymbol{O}, \end{aligned} \tag{9}$$

where $\boldsymbol{O}$ is the zero matrix. The real-valued Jacobian of the contact forces $\tilde{\boldsymbol{f}}_{nl}(\tilde{\boldsymbol{x}}_s^k)$ is computed as:

$$\nabla\tilde{\boldsymbol{f}}_{nl}(\tilde{\boldsymbol{x}}_s^k) = \begin{bmatrix} \frac{\partial \Re(\tilde{f}_{c,nl}(\tilde{\boldsymbol{x}}_{c,s}^k))}{\partial \Re(\tilde{\boldsymbol{x}}_{c,s}^k)} & \frac{\partial \Re(\tilde{f}_{c,nl}(\tilde{\boldsymbol{x}}_{c,s}^k))}{\partial \Im(\tilde{\boldsymbol{x}}_{c,s}^k)} \\ \frac{\partial \Im(\tilde{f}_{c,nl}(\tilde{\boldsymbol{x}}_{c,s}^k))}{\partial \Re(\tilde{\boldsymbol{x}}_{c,s}^k)} & \frac{\partial \Im(\tilde{f}_{c,nl}(\tilde{\boldsymbol{x}}_{c,s}^k))}{\partial \Im(\tilde{\boldsymbol{x}}_{c,s}^k)} \end{bmatrix}, \tag{10}$$

corresponding to the real-valued Jacobian of the complex nonlinear mapping expressed in terms of the real and imaginary components of $\tilde{\boldsymbol{x}}_{c,s}^k$. As detailed before the subscript $c$ refers to the complex-valued expression. Here and in the remainder of the paper, the operator $\nabla$ denotes the Jacobian matrix of first-order partial derivatives of a vector-valued function with respect to a vector argument.

3. Update of the displacement fields $\tilde{\boldsymbol{x}}_s^k$ and the Lagrange multipliers $\tilde{\lambda}$:

$$\begin{cases} \Delta\tilde{\boldsymbol{x}}_s^k = [\boldsymbol{D}_s(\omega) + \nabla\tilde{\boldsymbol{f}}_{nl}(\tilde{\boldsymbol{x}}_s^k)]^{-1}(-\boldsymbol{r}_{L,s}(\tilde{\boldsymbol{x}}_s^k, \tilde{\lambda}^k) - \boldsymbol{B}_s^T\tilde{\lambda}^k) \ \forall s = 1 \dots N, \\ \boldsymbol{F}_g^k\tilde{\lambda}^k = \boldsymbol{d}^k, \end{cases} \tag{11}$$

where:

$$\begin{aligned} \boldsymbol{F}_g^k &= -\sum_{s=1}^{N} \boldsymbol{B}_s[\boldsymbol{D}_s(\omega) + \nabla\tilde{\boldsymbol{f}}_{nl}(\tilde{\boldsymbol{x}}_s^k)]^{-1}\boldsymbol{B}_s^T, \\ \boldsymbol{d}^k &= -\sum_{s=1}^{N} \boldsymbol{B}_s([\boldsymbol{D}_s(\omega) + \nabla\tilde{\boldsymbol{f}}_{nl}(\tilde{\boldsymbol{x}}_s^k)]^{-1}\boldsymbol{r}_{L,s}(\tilde{\boldsymbol{x}}_s^k, \tilde{\lambda}^k) - \tilde{\boldsymbol{x}}_s^k), \end{aligned} \tag{12}$$

with $\boldsymbol{F}_g^k \in \mathbb{R}^{m\times m}$, $\boldsymbol{d}^k \in \mathbb{R}^m$ and the subscript $g$ denotes global quantities. The second equation in (11) is a linear system enforcing the compatibility of displacements at the interface nodes, here referred to as the interface problem. It is important to note that, unlike in the FETI framework (where a pseudoinverse is required) the dynamic stiffness matrix in frequency domain dynamic problems is generally non-singular. It becomes singular only when the excitation frequency $\omega$ coincides with a natural frequency of an undamped system. Since the mechanical systems are damped, the dynamic stiffness matrix is non-singular and therefore always invertible, justifying the use of a classical inverse. The next section describes the mathematical properties of the matrix $\boldsymbol{F}_g$ and outlines the procedure used to solve the interface problem.

### 2.2. Deflated interface problem

Considering (11), it should be noted that the first set of equations refers to local operations on the $s^{\text{th}}$ domain, whereas the second linear system involves quantities defined at the global system level. Since the interface problem spans multiple domains, its direct solution is computationally expensive in a parallel approach due to the need to exchange data among the domains and the overall size of the system. For this reason, an iterative solution combined with a matrix-free is used [20,22]. The matrix $\boldsymbol{F}_g^k$ can be written as:

$$\boldsymbol{F}_g^k = -\sum_{s=1}^{N} \boldsymbol{B}_s \left[ \begin{bmatrix} -\omega^2 \boldsymbol{M}_s + \boldsymbol{K}_s & -\omega \boldsymbol{C}_s \\ \omega \boldsymbol{C}_s & -\omega^2 \boldsymbol{M}_s + \boldsymbol{K}_s \end{bmatrix} + \nabla \tilde{\boldsymbol{f}}_{nl}(\tilde{\boldsymbol{x}}_s^k) \right]^{-1} \boldsymbol{B}_s^T. \tag{13}$$

It can be shown that $\boldsymbol{F}_g^k$ is neither symmetric nor positive definite (PD). This is due to the term $-\omega^2 \boldsymbol{M}_s + \boldsymbol{K}_s$, which may yield negative eigenvalues, since $\boldsymbol{M}_s$ is positive definite whereas $\boldsymbol{K}_s$ is only positive semi-definite. For an unconstrained domain, rigid body modes lead to zero eigenvalues in $\boldsymbol{K}_s$. Consequently, adding the term $-\omega^2 \boldsymbol{M}_s$, makes the matrix $-\omega^2 \boldsymbol{M}_s + \boldsymbol{K}_s$ indefinite. Such considerations lead to the conclusion that negative eigenvalues in $\boldsymbol{F}_g^k$ originate from:

1. Presence of unconstrained domains;
2. The value of the frequency at which (6) is solved;
3. The order of magnitude of the eigenvalues of $-\omega^2 \boldsymbol{M}_s$ relative to those of $\boldsymbol{K}_s$.

A well-established approach for the iterative solution of non-symmetric and indefinite systems is GMRES, a Krylov-subspace–based solver [26]. GMRES builds a Krylov subspace from the system matrix and, at each iteration, computes an approximate solution as a linear combination of the generated basis vectors that minimizes the residual norm. The distribution of eigenvalues strongly influences convergence: the less clustered the eigenvalues are, the more iterations are typically required. For indefinite matrices, negative eigenvalues further increase the risk of stagnation, often leading to a substantial growth in the iteration count. This occurs because negative eigenvalues cause GMRES to "oscillate" between negative and positive values, as GMRES constructs its Krylov basis using eigenvectors associated with the largest eigenvalues in module [26].

As previously discussed, the matrix $\boldsymbol{F}_g^k$ contains negative eigenvalues, which account for the large number of GMRES iterations observed. Moreover, as will be shown in Section 4.2, the iteration count increases with the excitation frequency $\omega$. To mitigate this effect, several strategies that exploit the spectral properties of the matrix have been proposed, including deflation methods [19,25,27,28]. The key idea behind deflation is to eliminate from the Krylov subspace those components that do not contribute effectively to the solution by introducing a projection matrix acting as a preconditioner. These vectors are typically collected into a matrix $\boldsymbol{G} \in \mathbb{R}^{m \times p}$ (with $p$ the number of retained vectors in the coarse space), commonly referred to as the coarse space (CS). In the following, we consider two variants of the matrix $\boldsymbol{G}$: a classical coarse space based on the rigid body modes ($\boldsymbol{G}_{RB}$) and a novel frequency based coarse space ($\boldsymbol{G}_{FB}$). The former variant is characterized by using rigid body modes, whereas the latter is based on the frequency properties of the system. These differences are reflected in their respective definitions and are used throughout the remainder of this section.

The deflation applied to the interface residual problem of (11) can then be written as:

$$\boldsymbol{G}^T \left( \boldsymbol{F}_g^k \tilde{\lambda}^k - \boldsymbol{d}^k \right) = \boldsymbol{o}. \tag{14}$$

From the physical point of view, the application of the coarse space $\boldsymbol{G}$, is equivalent to force the interface problem residual $\left( \boldsymbol{F}_g^k \tilde{\lambda}^k - \boldsymbol{d}^k \right)$ to be orthogonal to the deflated vectors contained in $\boldsymbol{G}$. Such an operation can be mathematically achieved by using the following projection which can be applied as a preconditioner:

$$\boldsymbol{P}^k = \boldsymbol{I} - \boldsymbol{F}_g^k \boldsymbol{G} \left( \boldsymbol{G}^T \boldsymbol{F}_g^k \boldsymbol{G} \right)^{-1} \boldsymbol{G}^T. \tag{15}$$

The entire solution process can be summarized in Algorithm 1, where the global and local computations are highlighted, and it is specified when and which communications happens. Matrix free approach is used and only required data are exchanged as detailed in [22]. It should be noted that to avoid the NR stagnation, a local step-length selection based on the Armijo condition is introduced in line 17 [29].

### 2.3. Rigid body modes coarse space

A common choice of a coarse space for the solution of structural dynamic problems in time domain is based on the use of the rigid body modes (RBCS) [18,20,22]:

$$\boldsymbol{G}_{RB} = \left[ \boldsymbol{B}_1 \begin{bmatrix} \boldsymbol{R}_1 & \boldsymbol{O} \\ \boldsymbol{O} & \boldsymbol{R}_1 \end{bmatrix} \cdots \boldsymbol{B}_{N_f} \begin{bmatrix} \boldsymbol{R}_{N_f} & \boldsymbol{O} \\ \boldsymbol{O} & \boldsymbol{R}_{N_f} \end{bmatrix} \right], \tag{16}$$

where $\boldsymbol{R}_s \in \mathbb{R}^{n_s \times p_s}$ (with $n_s$ and $p_s$ being the number of DOFs of the $s^{th}$ domain and the number of vectors retained in the coarse space, respectively), is the null space of the stiffness matrix $\boldsymbol{K}_s$, representing the rigid body modes of the $s^{th}$ domain. The subscript $f$ refers to floating domain meaning domain with singular $\boldsymbol{K}_s$, while $N_f$ is the number of floating

**Algorithm 1:** FETI Solution Scheme in a Nutshell.

1 **Given:** initial guesses $\tilde{\boldsymbol{x}}_s(\omega_0) = \boldsymbol{o}$, $\tilde{\lambda}(\omega_0) = \boldsymbol{o}$, and convergence criteria for the NR iterations.
// --- Local computation of $\boldsymbol{G}_s$ matrices ---
2 **for** $s = 1$ **to** $N$ **do**
3 Compute local matrix $\boldsymbol{G}_s$;
// --- Frequency sweep ---
4 **for** $i = 1$ **to** $N_{frequency\ points}$ **do**
// Initialize Newton-Raphson iteration
5 $\tilde{\boldsymbol{x}}_s(\omega_i)^1 = \tilde{\boldsymbol{x}}_s(\omega_{i-1})$, $\Delta\tilde{\boldsymbol{x}}_s^1 = \boldsymbol{o}$;
6 $\tilde{\lambda}(\omega_i)^1 = \tilde{\lambda}(\omega_{i-1})$, $\Delta\tilde{\lambda}^1 = \boldsymbol{o}$;
// Loop until convergence
7 **Set:** $k = 1$
8 **while** $\frac{\|\Delta\tilde{\boldsymbol{x}}_s(\omega_i)^k\|}{\|\tilde{\boldsymbol{x}}_s(\omega_i)^k\|}$ *and* $\frac{\|\Delta\tilde{\lambda}(\omega_i)^k\|}{\|\tilde{\lambda}(\omega_i)^k\|}$ *are not sufficiently small* **do**
// --- Local computations ---
9 Compute $\nabla\tilde{\boldsymbol{f}}_{nl}(\tilde{\boldsymbol{x}}_s^k)$ and $\tilde{\boldsymbol{f}}_{nl}(\tilde{\boldsymbol{x}}_s^k)$;
10 Compute local contributions $\boldsymbol{F}_s^k$ and $\boldsymbol{d}_s^k$;
// --- Global computations ---
11 Assemble of $\boldsymbol{G}^T \boldsymbol{F}_g^k \boldsymbol{G}$ by exchanging parts of $\boldsymbol{F}_s^k$ and $\boldsymbol{G}_s$;
12 Factorize $\boldsymbol{G}^T \boldsymbol{F}_g^k \boldsymbol{G}$;
13 Solve $\boldsymbol{P}^k \boldsymbol{F}_g^k \Delta\tilde{\lambda}_2^k = \boldsymbol{P}^k \boldsymbol{d}^k$ using GMRES;
14 $\Delta\tilde{\lambda}^k = \Delta\tilde{\lambda}_2^k + \boldsymbol{F}_g^k \boldsymbol{G} \left( \boldsymbol{G}^T \boldsymbol{F}_g^k \boldsymbol{G} \right)^{-1} \boldsymbol{G}^T \left( \boldsymbol{d}^k - \boldsymbol{F}_g^k \Delta\tilde{\lambda}_2^k \right)$;
// --- Local update ---
15 Compute $\Delta\tilde{\boldsymbol{x}}_s^k$;
16 Evaluate Armijo step size $\alpha_s$;
17 Update local displacements: $\tilde{\boldsymbol{x}}_s^{k+1} = \tilde{\boldsymbol{x}}_s^k + \alpha_s \Delta\tilde{\boldsymbol{x}}_s^k$;
// --- Global update ---
18 Update global Lagrange multipliers: $\tilde{\lambda}^{k+1} = \tilde{\lambda}^k + \Delta\tilde{\lambda}^k$;
19 **Update:** $k = k + 1$
// Store converged results for current frequency
20 **for** $s = 1$ **to** $N$ **do**
21 $\tilde{\boldsymbol{x}}_s(\omega_i) = \tilde{\boldsymbol{x}}_s^k$;
22 $\tilde{\lambda}(\omega_i) = \tilde{\lambda}^k$;

domains. The choice of $\boldsymbol{G}_{RB}$ has two main advantages:

- It can be computed only once since it does not depend on the frequency at which the response is computed;
- $p_s$ will be at least $2 \cdot 6 \cdot N_f$, where $N_f$ is the number of floating domains, 6 is the maximum number of rigid body modes, and the 2 accounts for using real algebra.

However, the $\boldsymbol{G}_{RB}$ coarse space does not account for the effect of $\omega$ on the eigenvalue distribution of $\boldsymbol{F}_g^k$. Increasing the frequency range of the analysis increases the number of negative eigenvalues in $\boldsymbol{F}_g^k$ that are no longer filtered by $\boldsymbol{G}_{RB}$, thus resulting in a larger number of GMRES iterations. To address this issue, we introduce the FBCS.

### 2.4. Frequency based coarse space

The physical meaning of the negative eigenvalues of the dynamic stiffness matrix $\boldsymbol{D}_s(\omega)$, which in turn generate negative eigenvalues in $\boldsymbol{F}_g^k$, is discussed first. In particular, if $\sigma$ and $\boldsymbol{v}$ denote the eigenvalue and eigenvector of $\boldsymbol{D}_s(\omega)$, the eigenvalue problem reads:

$$\begin{bmatrix} -\omega^2 \boldsymbol{M}_s + \boldsymbol{K}_s & -\omega \boldsymbol{C}_s \\ \omega \boldsymbol{C}_s & -\omega^2 \boldsymbol{M}_s + \boldsymbol{K}_s \end{bmatrix} \boldsymbol{v} = \sigma \boldsymbol{v}. \tag{17}$$

A negative eigenvalue $\sigma < 0$ implies that the external force ($\sigma \boldsymbol{v}$) produces a displacement in a direction opposite to that of the applied force. A similar interpretation applies to the inverse of the dynamic stiffness matrix, where $\boldsymbol{v}$ represents the Fourier coefficients of a force vector rather than those of a displacement field. The negative eigenvalues of $\boldsymbol{D}_s(\omega)$ arising from the zero eigenvalues of $\boldsymbol{K}_s$ (which correspond to rigid-body modes) can be effectively deflated not contributing to the solution. Expanding to $\boldsymbol{F}_g$, eigenvectors associated with negative eigenvalues of $\boldsymbol{F}_g$ can be removed (by means of the projection), which may improve the convergence of GMRES. In cases where computing the eigenvalues and eigenvectors of $\boldsymbol{F}_g$ is feasible, constructing the FBCS $\boldsymbol{G}_{FB}$ is straightforward: after identifying the eigenvalues corresponding to the eigenvectors to be deflated, the latter are used to build the coarse space (i.e., they are assembled as the columns of $\boldsymbol{G}_{FB}$). However, since $\boldsymbol{F}_g$ is large and shared across the domains, directly solving its eigenproblem is computationally impractical.

The objective is therefore to find a way to obtain the eigenvectors associated with $\boldsymbol{F}_g$ without explicitly computing its eigenvalues. To do so, we consider the expression of $\boldsymbol{F}_g$ at the $k^{\text{th}}$ NR iteration:

$$\boldsymbol{F}_g^k = -\sum_{s=1}^{N} \boldsymbol{B}_s \left[ \boldsymbol{D}_s + \nabla \tilde{\boldsymbol{f}}_{nl}(\tilde{\boldsymbol{x}}_s^k) \right]^{-1} \boldsymbol{B}_s^T. \tag{18}$$

Assuming for a moment to consider the linear case (in the next section, it is discussed why this assumption can hold), meaning $\nabla \tilde{\boldsymbol{f}}_{nl}(\tilde{\boldsymbol{x}}_s^k)$ is constant:

$$-\sum_{s=1}^{N} \boldsymbol{B}_s \begin{bmatrix} -\omega^2 \boldsymbol{M}_s + \boldsymbol{K}_{s,a} & -\omega \boldsymbol{C}_s \\ \omega \boldsymbol{C}_s & -\omega^2 \boldsymbol{M}_s + \boldsymbol{K}_{s,a} \end{bmatrix} \boldsymbol{B}_s^T = -\sum_{s=1}^{N} \boldsymbol{B}_s \boldsymbol{D}_{s,a}^{-1} \boldsymbol{B}_s^T, \tag{19}$$

where $\boldsymbol{D}_{s,a}$ is the dynamic stiffness matrix computed under the assumption that the contact remains closed (i.e., the Jacobian of the contact forces is constant) partitioned into real and imaginary parts. To evaluate the eigenvalue distribution of $\boldsymbol{F}_g^k$, the idea is to approximate it using the spectrum of the local quantities $\boldsymbol{B}_s \boldsymbol{D}_{s,a}^{-1} \boldsymbol{B}_s^T$, and then select the eigenvectors to include in the coarse space. Focusing on this local quantity, the connectivity matrices $\boldsymbol{B}_s$ act by selecting the degrees of freedom (DOFs) of the $s^{\text{th}}$ domain that are associated with Lagrange multipliers. Consequently, $\boldsymbol{B}_s$ can be partitioned as follows:

$$\boldsymbol{B}_s = \begin{bmatrix} \boldsymbol{B}_{LI,s} & \boldsymbol{O} \\ \boldsymbol{O} & \boldsymbol{O} \end{bmatrix}, \tag{20}$$

where the subscript $LI$ refers to the partition having the rows associated with the Lagrange multipliers of the $s^{th}$ domain and the columns associated with the DOFs to which they are connected. The zero matrices $\boldsymbol{O}$ are rectangular matrices having a shape consistent with $\boldsymbol{B}_s$. Similarly $\boldsymbol{D}_{s,a}$ (before being partitioned into real and imaginary parts) can be partitioned in DOFs connected to Lagrange multipliers (subscript $I$) and other DOFs (subscript $O$):

$$\boldsymbol{D}_{s,a}^{-1} = \begin{bmatrix} \boldsymbol{D}_{II,s} & \boldsymbol{D}_{IO,s} \\ \boldsymbol{D}_{OI,s} & \boldsymbol{D}_{OO,s} \end{bmatrix}^{-1} = \begin{bmatrix} \boldsymbol{H}_{II,s} & \boldsymbol{H}_{IO,s} \\ \boldsymbol{H}_{IO,s} & \boldsymbol{H}_{OO,s} \end{bmatrix}, \tag{21}$$

where, $\boldsymbol{H}$ denotes the resulting blocks in the inverse of $\boldsymbol{D}_{s,a}$. Combining (20) with (21) results in:

$$\boldsymbol{B}_s \boldsymbol{D}_{s,a}^{-1} \boldsymbol{B}_{sT} = \begin{bmatrix} \boldsymbol{B}_{LI,s} \boldsymbol{H}_{II,s} \boldsymbol{B}_{LI,s}^T & \boldsymbol{O} \\ \boldsymbol{O} & \boldsymbol{O} \end{bmatrix}. \tag{22}$$

The idea is to approximate the spectrum of (19) as a combination of the spectrum of the matrices in (22), which in turn can be reduced to the spectrum of $\boldsymbol{B}_{LI,s} \boldsymbol{H}_{II,s} \boldsymbol{B}_{LI,s}^T$. The restricted connectivity matrices $\boldsymbol{B}_{LI,s}$ can be viewed as identity matrices with some additional repeated rows (due to redundancies in the Lagrange multipliers), which result in duplicated eigenvalues in the spectrum of $\boldsymbol{B}_{LI,s} \boldsymbol{H}_{II,s} \boldsymbol{B}_{LI,s}^T$. For this reason, when evaluating the spectral distribution, they can be approximated as identity matrices. In summary, the spectrum of each term in (19) can be approximated by the spectrum of $\boldsymbol{H}_{II,s}$.

Up to this point, no information has been provided about $\boldsymbol{H}_{II,s}$. It can be shown that $\boldsymbol{H}_{II,s}$ represents the Schur complement of (21):

$$\boldsymbol{H}_{II,s} = \left[ \boldsymbol{D}_{II,s} - \boldsymbol{D}_{IO,s} \boldsymbol{D}_{OO,s}^{-1} \boldsymbol{D}_{OI,s} \right]^{-1}. \tag{23}$$

Before continuing into the spectrum evaluation of $\boldsymbol{H}_{II,s}$, let's consider the dynamic stiffness matrix $\boldsymbol{D}_{s,a}$ that, when partitioned into real and imaginary parts as in (19), it has a structure of the type:

$$\begin{bmatrix} \boldsymbol{S} & -\boldsymbol{N} \\ \boldsymbol{N} & \boldsymbol{S} \end{bmatrix}, \tag{24}$$

where $\boldsymbol{S}$ and $\boldsymbol{N}$ are real symmetric square matrices. It can be shown (by performing algebraic computations that exploit the structure of these matrices) that (23) also has the same shape. This shape makes it possible to state:

- The real part of the eigenvalues of such a matrix is bounded by the real eigenvalues of the $\boldsymbol{S}$ block;
- The imaginary part of the eigenvalues is bounded by the imaginary eigenvalues of the $\boldsymbol{N}$ block.

Since the goal of the spectral evaluation is to identify and deflate eigenvectors associated with eigenvalues that should not enter the Krylov subspace the analysis can be restricted to the computation of the spectrum of the $\boldsymbol{S}$ block, meaning the real part of the eigenvalues. The reason why the analysis can be limited to real eigenvalues is because the imaginary part (outer diagonal blocks) arises from the damping which is some order of magnitude lower than the main diagonal terms. Summing up, the construction of the FBCS can be summarized in Algorithm 2, where the subscript $s$ is used to refer to the $s^{th}$ domain. At the beginning of this section two assumptions has been done:

1. The linear case has been considered to write Eq. (19);
2. A fixed frequency point $\omega$ has been considered.

Regarding the first point, since the nonlinearity is localized and the additional term $\nabla \tilde{\boldsymbol{f}}_{nl}(\tilde{\boldsymbol{x}}_s^k)$ in (18) is a low-rank matrix not present in all domains, the FBCS defined for the linear case is also effective for the nonlinear case. Concerning the second point, from an engineering perspective, nonlinear forced responses are typically computed over relatively narrow frequency ranges. Consequently, the variation of $\omega$ within this range does not significantly affect the CS, and its construction can therefore use the mean value of the frequency range.

**Algorithm 2:** Frequency Based Coarse Space in a Nutshell.

Given $\boldsymbol{F}_g^k = -\sum_{s=1}^{N} \boldsymbol{B}_s \boldsymbol{D}_{s,a}^{-1} \boldsymbol{B}_s^T$

**for** $s = 1 \dots N$ **do**

  $\boldsymbol{B}_s \boldsymbol{D}_{s,a}^{-1} \boldsymbol{B}_s^T$ is approximated with:

  $$\boldsymbol{H}_{II,s} = \left[\boldsymbol{D}_{II,s} - \boldsymbol{D}_{IO,s}\boldsymbol{D}_{OO,s}^{-1}\boldsymbol{D}_{OI,s}\right]^{-1} = \begin{bmatrix} \boldsymbol{S}_s & -\boldsymbol{N}_s \\ \boldsymbol{N}_s & \boldsymbol{S}_s \end{bmatrix}$$

  The eigenvalues and eigenvectors of $\boldsymbol{S}_s$ are computed

  The eigenvectors to be deflated are stored into $\boldsymbol{R}_{FB,s}$

$\boldsymbol{G}_{FB} = \left[\boldsymbol{B}_1 \begin{bmatrix} \boldsymbol{R}_{FB,1} & \boldsymbol{O} \\ \boldsymbol{O} & \boldsymbol{R}_{FB,1} \end{bmatrix} \cdots \boldsymbol{B}_N \begin{bmatrix} \boldsymbol{R}_{FB,N} & \boldsymbol{O} \\ \boldsymbol{O} & \boldsymbol{R}_{FB,N} \end{bmatrix}\right]$

Up to now, the criterion for selecting eigenvectors for deflation has consisted of choosing those associated with negative eigenvalues. Although this approach removes negative eigenvalues from $\boldsymbol{F}_g^k$ and thereby accelerates GMRES convergence, further deflation can be beneficial. From an engineering standpoint, and considering the typical frequency ranges analyzed, eigenvectors associated with large eigenvalues may also be excluded, as they do not contribute meaningfully to the solution. For this reason, the eigenvectors selected for deflation include both those associated with negative eigenvalues and those with eigenvalues larger than a specified tolerance, which is problem dependent. It is important to note that if the term $\omega^2$ does not significantly influence the matrix $-\omega^2 \boldsymbol{M}_s + \boldsymbol{K}_s$, the FBCS becomes equivalent to the RBCS. In such cases, adopting the RBCS leads to the deflation of vectors that are effectively equivalent to the rigid body modes. As demonstrated in Section 4.1, for a fixed frequency $\omega$, the convergence of GMRES is also influenced by the number of domains.

## 3. Implementation

The scope of this section is to address the implementation of the developed method and to provide an insight on the domain decomposition strategy as well as the contact model used.

### 3.1. Parallel implementation and FE decomposition

An important role in the achievable computational efficiency of the method, is played by the partitioning process of the FE model. The decomposition procedure is performed using the METIS library where the FE model is considered as a graph having as vertices and edges the FE nodes and elements, respectively [30]. Since METIS operates on a single connected mesh, the contacting bodies were temporarily treated as a single domain by enforcing connectivity at the contact interfaces, allowing to generate domains spanning both bodies. Then a weighting procedure is applied to partition the graph satisfying the following conditions:

- Balanced domains size in terms of number of DOFs;
- Minimization of the Lagrange multipliers;
- Distribution of the nonlinearities.

The satisfaction of the previous criterions has the aim of balancing the computational cost on each domain and minimize the communication among them. From the Algorithm 1, as stated in Section 2.2, it can be noted that the solution process consists of local and global operations, resulting in the following dual level parallelization:

1. Local operations are parallelized using a multithread approach based on OpenMP protocol, using the Eigen library to manage matrix operations [31];
2. Global operations are parallelized using a multiprocessing approach based on OpenMPI and the PETSc library [32].

This dual level parallelization allows to achieve a good efficiency in the parallel implementation as demonstrated by the strong scalability analyses in [22].

As explained in Section 2.2 a crucial point in the solution process is given by the introduction of the coarse space to accelerate the GMRES convergence. Assuming that $\boldsymbol{G}$ is available, the preconditioner $\boldsymbol{P}^k$ in (15) should be constructed. However the direct assembly of $\boldsymbol{P}^k$ is computationally inefficient due to its size and because it involves global quantities. For this reason matrix-free approach is used, where matrices in the summation are stored at domain level and only vectors are exchanged between processes, as detailed in [20,22]. This involves the least number of information exchange between different processes, each of which operates on a specific domain. In such way, the information exchanged only consists of the partitions of $\boldsymbol{R}_s$ to be used either in $\boldsymbol{G}_{RB}$ and $\boldsymbol{G}_{FB}$. An important point is the computational time needed to build the FBCS $\boldsymbol{G}_{FB}$ with respect to the RBCS $\boldsymbol{G}_{RB}$. It should be noted that the $\boldsymbol{H}_{II,s}$ matrix (used to compute $\boldsymbol{R}_{FB,s}$) has a size equal to the number of DOFs associated with Lagrange multipliers, while the $\boldsymbol{K}_s$ matrix (used to compute $\boldsymbol{R}_s$) has a size equal to the number of DOFs of the $s^{th}$ domain which are larger than the previous ones. This results in a less computational time needed to compute the eigenvalues of the $\boldsymbol{S}_s$ block. In both cases eigenvalue computation is performed using a direct approach. Moreover, the Schur complement of (23) must be computed leading to a comparable computational time between the two coarse spaces. This shows how the novel proposed CS does not introduce computational inefficiency or bottlenecks with respect to the standard rigid body modes coarse space. Regarding the eigenvalues computation it should be noted that give a frequency range of the analysis they are computed only once at the beginning at domain levels and stored at domain level. Matrix inverses are never directly computed since they are only factorized once, stored and used at domain level.

### 3.2. Contact model

To model the friction interfaces, a contact model based on the penalty approach is used. The first order Fourier coefficients of the nonlinear contact forces $\tilde{\boldsymbol{f}}_{nl}(\tilde{\boldsymbol{x}}_s^k)$ and the Jacobian $\nabla\tilde{\boldsymbol{f}}_{nl}(\tilde{\boldsymbol{x}}_s^k)$ are computed using a 3D contact model with uncoupled tangential motion based on the Alternating Frequency/Time (AFT) method [33,34]. We remind the reader that the Jacobian $\nabla\tilde{\boldsymbol{f}}_{nl}(\tilde{\boldsymbol{x}}_s^k)$ defined in Section 2.1, corresponds to the real-valued Jacobian of the complex nonlinear mapping expressed in terms of the real and imaginary components of $\tilde{\boldsymbol{x}}_{c,s}^k$, as defined in (10). A schematic representation of the contact model is shown in Fig. 3. The relative displacements between the contact nodes are denoted by $u_x$, $u_y$, and $u_z$, while the displacement of the slider is represented by $w_x$, $w_y$, and $w_z$. The contact preload and the friction coefficient at the interface are denoted by $N$ and $\mu$, respectively. The contact stiffness in the three

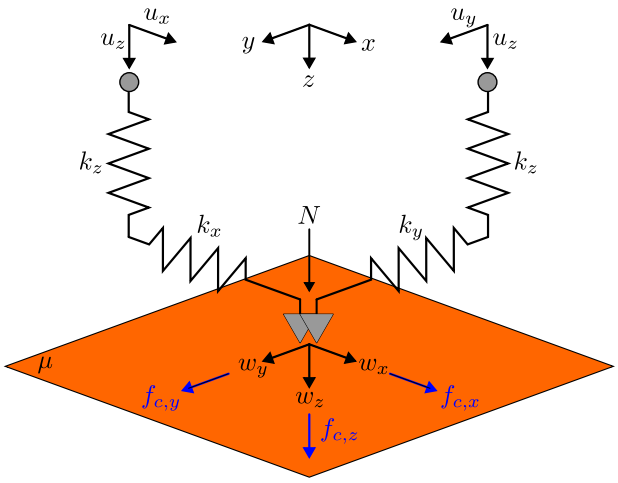


**Fig. 3.** Contact elements referred to One node.

spatial directions is represented by $k_x$, $k_y$, and $k_z$. Since the AFT procedure involves the application of the Fast Fourier Transform and its inverse, the FFTW library is employed for this purpose.

## 4. Results

The objective of this section is to demonstrate how the proposed FBCS improves the computational efficiency (in terms of computational times and GMRES iterations) of the methodology used for predicting the forced response of an FE model of bladed disks in the presence of frictional contact at the fir-tree joints between each blade and disk slot.

First, a weak scalability analysis is performed on a simple FE model, comparing the RBCS with the FBCS. Then, the effect of the excitation frequency $\omega$ is examined. All the analyses are carried out on the LEONARDO supercomputer, owned by the EuroHPC Joint Undertaking, hosted by CINECA (Italy) [35]. The LEONARDO DCGP partition is used, consisting of 1536 nodes, each equipped with two Intel Xeon Platinum 8480+ processors, providing a total of 112 cores per node and 512 GB of RAM. The Intel oneAPI MPI compiler and PETSc 3.20.1 are used.

### 4.1. Weak scalability analysis and effect on GMRES convergence

To assess the performance of the newly proposed FBCS compared to the RBCS, a weak scalability analysis is performed. This analysis involves fixing the size of each domain (in terms of DOFs) used in the decomposition of the FE model (which does not have a fixed overall size), and evaluating how the computational time changes as the number of domains increases. Increasing the number of domains increases the size of the overall problem to be solved [36].

For this purpose, an FE model of a cube consisting of two constrained bodies in contact with each other is used. The FE model is decomposed using the METIS software [22,30], a tolerance of $10^{-7}$ (prescribed on both the primal and dual variables) is used for NR iterations and a tolerance of $10^{-6}$ is used for stopping GMRES convergence. The physical dimensions of the model are kept fixed, while the mesh is adapted to maintain an approximately constant domain size as the number of domains increases. All analysis parameters, including the frequency $\omega$, are kept constant across different decompositions. To assess the effect of the FBCS and RBCS two problem sizes are evaluated:

- Case 1: domain size of about $1.2{\cdot}10^3$ DOFs and maximum FE model size of $1.3{\cdot}10^5$ DOFs;
- Case 2: domain size of about $11{\cdot}10^3$ DOFs and maximum FE model size of $1.2{\cdot}10^6$ DOFs;

It should be noted that, since the equations are solved in real algebra, the problem size seen by the solver is doubled. This means that, for Case 1, the domain size is $2.4 \cdot 10^3$ and the maximum problem size is $2.6{\cdot}10^5$, whereas for Case 2, the domain size is $22{\cdot}10^3$ and the maximum problem size is $2.4 \cdot 10^6$. Table 1 reports the number of domains $N$, the average number of DOFs per domain (DOFs/domain), the size of the interface problem $\tilde{\lambda}$) DOFs), the number of HPC nodes allocated (Nodes), the number of MPI processes (Proc.) and number of CPUs used by each process (CPUs/Proc.).

**Table 1**
Weak scalability parameters for case 1 (C1) and case 2 (C2).

| $N$ | DOFs/domain | | $\tilde{\lambda}$ DOFs | | Nodes | | Proc. | | CPUs/proc. | |
|---|---|---|---|---|---|---|---|---|---|---|
| | C1 | C2 | C1 | C2 | C1 | C2 | C1 | C2 | C1 | C2 |
| 16 | 1234 | 11,048 | 5913 | 29,019 | 1 | 1 | 16 | 16 | 2 | 4 |
| 32 | 1263 | 10,652 | 14,013 | 61,419 | 1 | 2 | 32 | 16 | 2 | 4 |
| 64 | 1201 | 10,962 | 28,110 | 136,233 | 2 | 4 | 32 | 16 | 2 | 4 |
| 112 | 1180 | 10,926 | 51,168 | 252,618 | 2 | 4 | 56 | 28 | 2 | 4 |

In Fig. 4 it is reported that the FE model used for the weak scalability analysis of Case 1, shows how the mesh size changes with the changing number of domains. To assess the weak scalability, the efficiency $\eta$ is defined as follows:

$$\eta = \frac{T(N_{ref})}{T(N)}, \tag{25}$$

where $T(N_{\text{ref}})$ is the computational time for a given operation associated with the decomposition into $N_{\text{ref}}$ domains (16), and $T(N)$ is the computational time for the same operation associated with the decomposition into $N$ domains. Since the objective of the weak scalability analysis is to assess the performance of the method, the evaluation is performed at only one frequency point $\omega$.

In Fig. 5, the weak scalability analysis for Case 1 is shown on the left in terms of $\eta$ and on the right in terms of runtime, comparing the RBCS and FBCS. The global operations include the time required for assembling and factorizing the global part of the projection operator ($\boldsymbol{G}^T \boldsymbol{F}_g^k \boldsymbol{G}$), solving the interface problem with GMRES, and the data exchange among processes. The local operations include the computation of the contact model (CM), and the computation of the local quantities $\boldsymbol{F}_s^k$ and $\boldsymbol{d}_s^k$. The total operations are referred to the total runtime given a frequency point and an NR iteration. In Fig. 6 the same analyses are reported for Case 2.

Comparing the two plots, local operations maintain about the same efficiency, which is justified by the constant size of the individual domains. A difference can be observed in the global operations, which in turn affect the total efficiency. The proposed FBCS maintains global efficiency higher than 60% with 112 domains and higher than 70% with the other configurations for Case 1. On the other hand, the RBCS causes the global efficiency to rapidly decrease, dropping to 30% with 112 domains for Case 1, which is justified by the time required for GMRES to converge. For Case 2, however, a smaller difference can be observed between the RBCS and FBCS approaches in terms of efficiency. Even so, the FBCS approach requires much less computational time compared to the RBCS. The primary factor affecting the total runtime is the number of GMRES iterations required for convergence. The reduction in iterations achieved by the FBCS explains why it consistently requires less computational time. In contrast, the effectiveness of the RBCS diminishes as the number of domains increases (as discussed later), leading to a corresponding decrease in efficiency, whereas the FBCS maintains its effectiveness regardless of the number of domains.

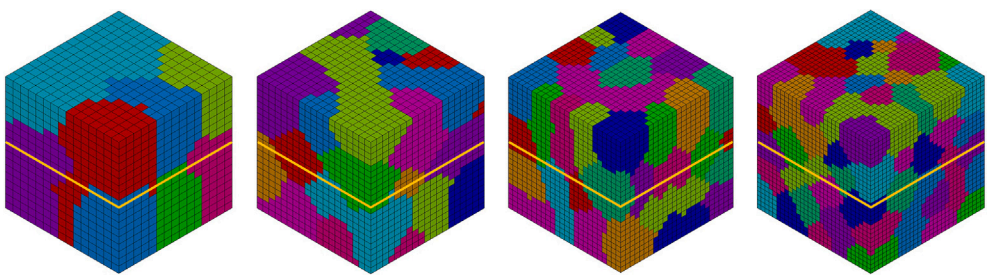

**Fig. 4.** FE model decomposition used for the weak scalability analysis.

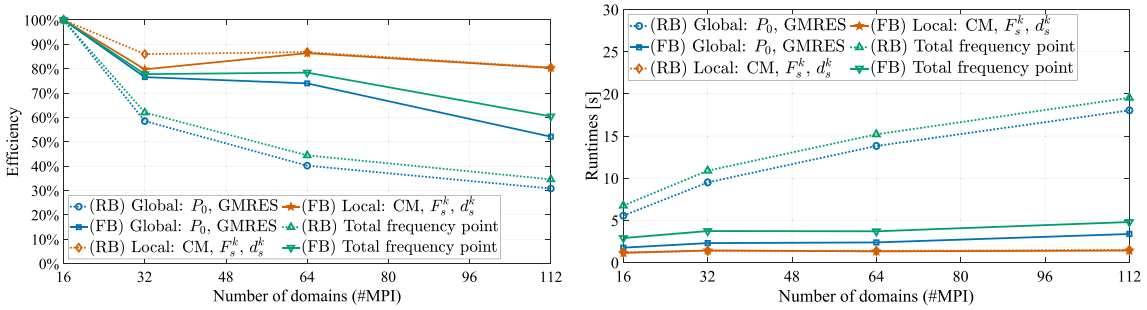


**Fig. 5.** Weak scalability analysis with the RBCS and the FBCS case 1.

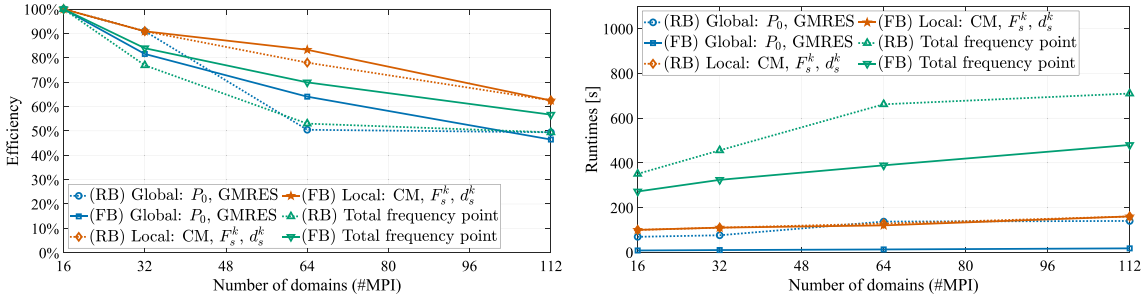


**Fig. 6.** Weak scalability analysis with the RBCS and the FBCS case 2.

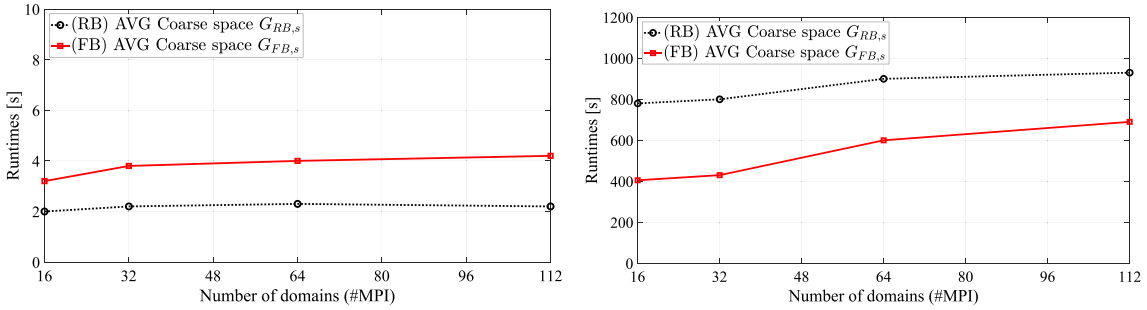


**Fig. 7.** RBCS with the FBCS coarse space construction case 1 (left) and case 2 (right).

The preprocessing steps (consisting of the decomposition of the FE model) are not reported since they are negligible compared to the runtimes requested by the computation of the response over a frequency range, being in the order of 5-10s and 20-90s for Case 1 and Case 2, respectively. The preprocessing time is negligible because it is performed only once. Since the computation is carried out at multiple frequency points (on the order of 100) and over several NR iterations, the total runtime scales with the number of frequency points and iterations, while the preprocessing cost remains unchanged. An important role in the solution process is played by the one step required to build the $\boldsymbol{G}_s$ matrices. It is important to note that this computation is performed only once at the beginning of the forced response computation. In Fig. 7, the average runtimes over domains to build $\boldsymbol{G}_s$ for Case 1 and Case 2 are reported. As can be seen from the plots, for Case 1, due to the small sizes of the domains, the times are comparable, while for Case 2, the time required by the FBCS approach is smaller. This is because, in the FBCS, eigenvalues are computed on the Schur complement of the domain matrix, which has a smaller size compared to the full matrix used by the RBCS, meaning that the significant difference in the computational times is primarily due to the eigenvectors computation. For the FBCS the inverse matrix factors are computed using self adjoint eigendecomposition, while for the RBCS they are computed using the full singular value decomposition via a bidiagonal divide and conquer SVD algorithm.

In Fig. 8, the number of GMRES iterations required using the RBCS and FBCS for Case 1 and Case 2 are compared. As can be seen from the plots, the number of GMRES iterations increases as the number of domains increases when using the RBCS. On the other hand, the adoption of the FBCS results in the GMRES iterations remaining nearly constant and considerably lower than in the previous case for both Case 1 and Case 2. The reason why the number of domains affects the GMRES iterations when the RBCS is used, while keeping the FE model size and the frequency $\omega$ fixed, can be found in the term $-\omega^2 \boldsymbol{M}_s + \boldsymbol{K}_s$. This is because, even though $\omega$ is fixed, the ratio in the order of magnitude between $\boldsymbol{M}_s$ and $\boldsymbol{K}_s$ changes, introducing the possibility of additional negative eigenvalues that are not captured by the RBCS, as explained in Section 2.4. A final remark is provided comparing the memory consumption requested by the FBCS and RBCS for Case 1 and Case 2, reported in Table 2. As can be seen from Table 2, both the RBCS and FBCS require the same amount of RAM, proving that given the same resources required the FBCS is more efficient from the computational point of view. It should be noted that on systems with more limited memory, the runtime and scalability could differ from the results reported here. A more detailed assessment

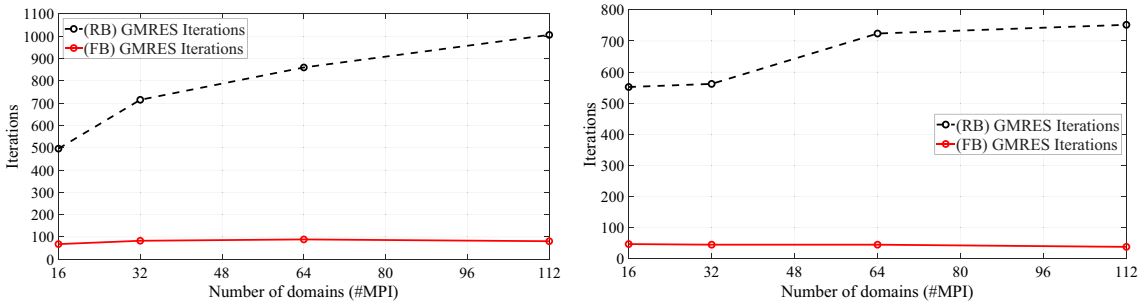


**Fig. 8.** GMRES iterations with the RBCS and the FBCS for case 1 (left) and case 2 (right).

**Table 2**
Memory consumption for Case 1 and Case 2 at different decompositions.

| | Maximum RAM [MB]/process | | | |
|---|---|---|---|---|
| | N16 | N32 | N64 | N112 |
| Case 1 (RBCS) | 448 | 472 | 459 | 527 |
| Case 1 (FBCS) | 490 | 375 | 368 | 579 |
| Case 2 (RBCS) | 11,838 | 12,124 | 12,969 | 12,960 |
| Case 2 (FBCS) | 13,729 | 14,618 | 15,584 | 15,174 |

of memory usage and performance on HPC systems could be considered in future work. In the next section, the effect of $\omega$ is analyzed for a fixed FE model and domain decomposition.

### 4.2. Effect of the frequency on GMRES convergence

As explained in Section 2.2, the parameter $\omega$ in (13) affects the eigenvalue distribution, leading to negative eigenvalues and making the RBCS ineffective. To analyze how the proposed FBCS mitigates this phenomenon, an FE model of a full bladed disk with a fir-tree contact at the blade root is considered. The model consists of 40 sectors, with a total of 507,480 DOFs, of which 23,760 correspond to the contact interfaces where frictional nonlinearity occurs. The material used has a Young's Modulus of $2 \cdot 10^{11}$ N/m$^2$, a density of 7800 kg/m$^3$, and a Poisson's ratio of 0.3. The FE model is decomposed into 224 domains, leading to $\tilde{\lambda}$ 179,652 DOFs, solved with 2 CPUs assigned per domain to maximize the utilization of each LEONARDO node (each node consists of 112 CPUs). The model is meshed using ANSYS Mechanical APDL using SOLID185 elements. The FE model is decomposed using the METIS software [22,30]. A tolerance of $10^{-7}$ (prescribed on both the primal and dual variables) is adopted for the Newton–Raphson iterations. For the GMRES solver, a tolerance of $10^{-4}$ is used in this example to illustrate the convergence behavior, while a stricter tolerance of $10^{-6}$ is employed in the actual simulations presented in the following sections.

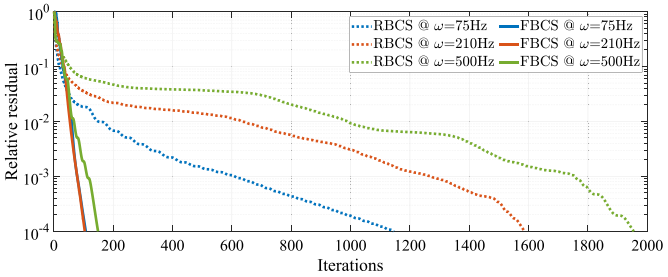


**Fig. 10.** GMRES convergence at three different frequency points with the RBCS and the FBCS.

In Fig. 9, the following are shown, from left to right: the single sector focusing on the contact areas (highlighted in orange), the full bladed disk, and the decomposed bladed disk.

To assess the effect of the parameter $\omega$, the GMRES convergence associated with the first NR iterations at three different frequency points is analyzed. The analysis is conducted by linearizing the contact forces, which involves treating the contact model as a linear spring connecting two homologous points on either side of the contact interface (i.e., $\nabla \tilde{\boldsymbol{f}}_{nl,s}(\tilde{\boldsymbol{x}}_s)$ is constant). The analysis is performed near three resonance frequencies, which are excited by a periodic excitation applied at the blade tip of each sector. The selected frequency points are 75 Hz, 210 Hz, and 500 Hz, which are close to the resonance peaks occurring at 78 Hz, 212 Hz, and 511 Hz. It is important to note that only the first NR iteration is considered because it is the most relevant one, given that each frequency point starts with a zero vector initial guess.

In Fig. 10 it is reported a comparison between the GMRES convergence at the three different frequency points comparing the RBCS with the

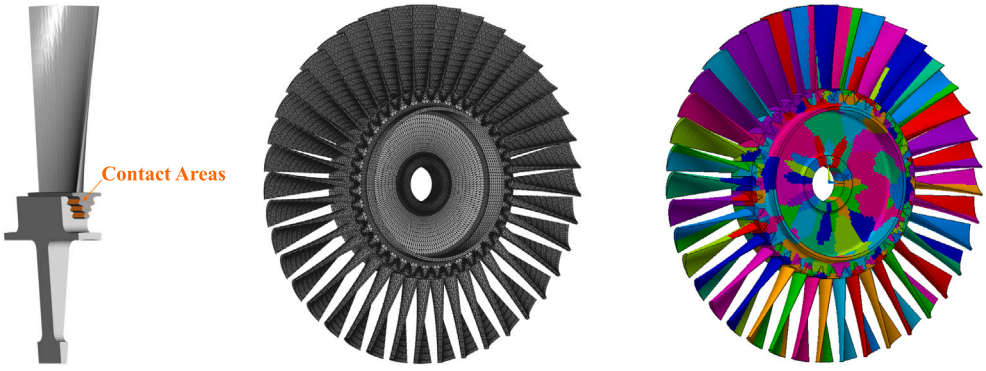


**Fig. 9.** From left to the right: single sector, full bladed disk and domain decomposition.

FBCS. As can be noticed from the figure, increasing the frequency point from 75 Hz to 500 Hz makes the RBCS ineffective doubling the number of GMRES iterations to about 2000 iterations. Instead the FBCS (where some higher eigenvalues are also deflated as explained in Section 2.4) keeps the iteration at around 150, mitigating the effect of the increase in $\omega$ and reducing the GMRES.

### 4.3. Forced response of a full tuned bladed disk

The first objective of this section is to validate the proposed FBCS on a nonlinear forced response analysis of a tuned bladed disk, comparing the computed response with state-of-the art approaches based on ROMs. The FE model introduced in Section 4.2 is used with the same decomposition into 224 domains. The FE model is decomposed using the METIS software [22,30], a tolerance of $10^{-7}$ is used for NR iterations and a tolerance of $10^{-6}$ (prescribed on both the primal and dual variables) is used for stopping GMRES convergence. The analyses are executed introducing a proportional damping model (meaning $\boldsymbol{C} = \alpha\boldsymbol{M} + \beta\boldsymbol{K}$) with $\alpha = 3$ and $\beta = 0$ and a traveling wave excitation of 1.5 N at engine order (EO) 3 applied at two nodes of each blade tip. The settings used for the analyses are not restricted by any specific choice; different settings can be applied, as they do not affect the proposed methodology. A preload $N$ of 200 N is applied on each contact node.

In Fig. 11 are reported on the left the nonlinear forced response in the frequency range between 76.5 Hz and 79.5 Hz while on the right the nonlinear forced response in the range between 501.5 Hz and 504.5 Hz. On the x axis the frequency of the analysis, while on the left y-axis the response amplitudes computed at the same DOF for all the blades. In all the subsequent figures, the following abbreviations are used: Linear Forced Response (LFR), Nonlinear Forced Response (NFR), Cyclic ROM (CYC ROM), Rigid Body (RB) and Frequency Based (FB).
The grey curve is the linear forced response. To validate the computed responses, the NOVA© software by Politecnico di Torino is used, which performs the same analysis on a Craig-Bampton reduced order model [3] of the bladed disk, obtained by retaining as master nodes the contact nodes and the excited nodes. The analysis is performed, and then, the cyclic symmetry boundary conditions are imposed at the interface between the different sectors. The nonlinear forced response is then computed using the FETI method with both the RBCS and the FBCS. As can be seen from Fig. 11 the responses computed with the three approaches perfectly overlap for both the frequency ranges of the analysis, proving the validity of the newly introduced coarse space.

In Fig. 12 the number of GMRES iterations related to the first NR iteration of the nonlinear forced response in the frequency range between 76.5 Hz and 79.5 Hz is reported on the left, while on the right, the GMRES iterations related to the first NR iteration of the nonlinear forced response in the range between 501.5 Hz and 504.5 Hz.

Focusing on the nonlinear forced response analysis in the lower frequency range (between 76.5 Hz and 79.5 Hz), as shown in Fig. 12, the use of the FBCS reduces the number of GMRES iterations by a factor of about 3 compared to the RBCS. Moving to a higher frequency range (between 501.5 Hz and 504.5 Hz), the impact of the FBCS becomes more significant, reducing GMRES iterations by approximately a factor of 10. This demonstrates that as the frequency increases, the RBCS loses its effectiveness, while the proposed coarse space remains effective.

In Fig. 13, the GMRES time related to the first NR iteration of the nonlinear forced response in the frequency range between 76.5 Hz and 79.5 Hz is shown on the left, while on the right, the GMRES time for the first NR iteration in the frequency range between 501.5 Hz and 504.5 Hz is reported. Since GMRES is performed at each frequency point and during each NR iteration, it is straightforward to conclude how this affects the overall computational time.

In Fig. 14 the number of NR iterations related to nonlinear forced response in the frequency range between 76.5 Hz and 79.5 Hz is reported on the left, while on the right, the number of NR iterations related to the nonlinear forced response in the range between 501.5 Hz and 504.5 Hz. As can be seen from the plots, the introduction of the new FBCS does not affect the number of NR iterations needed to converge.

Focusing on the nonlinear forced response in the frequency range between 76.5 Hz and 79.5 Hz the use of the FBCS reduces the computational time of about the 25%, while in the frequency range

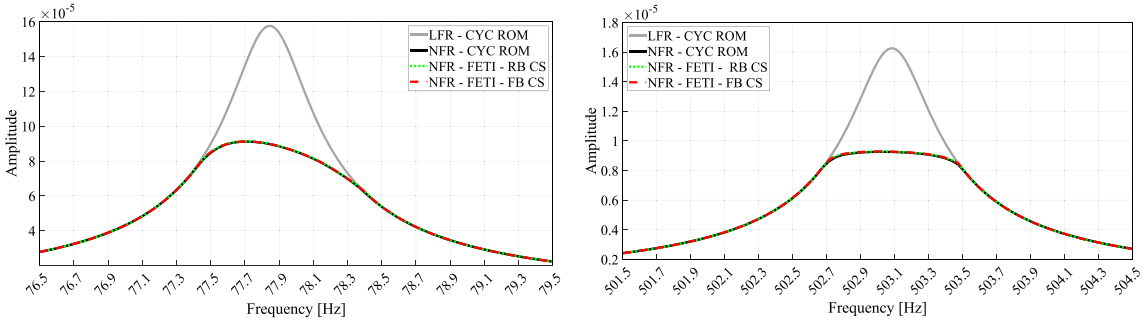


**Fig. 11.** Forced response analysis at EO 3 between 76.5 Hz and 79.5 Hz (left) and between 501.5 Hz and 504.5 Hz (right).

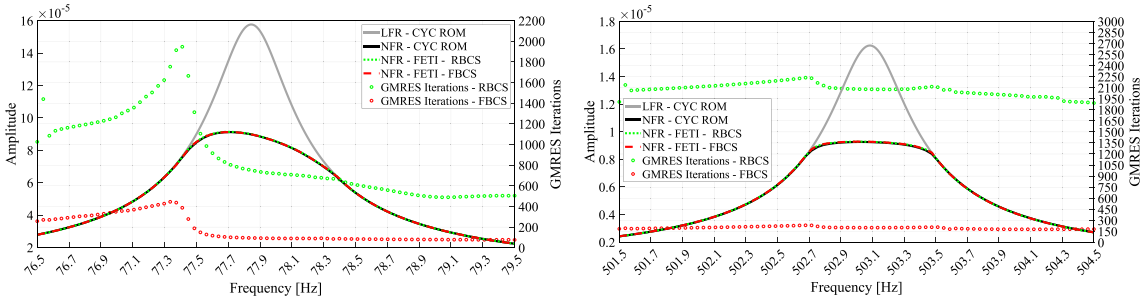


**Fig. 12.** GMRES iterations referred to nonlinear forced response between 76.5 Hz and 79.5 Hz (left) and between 501.5 Hz and 504.5 Hz (right).

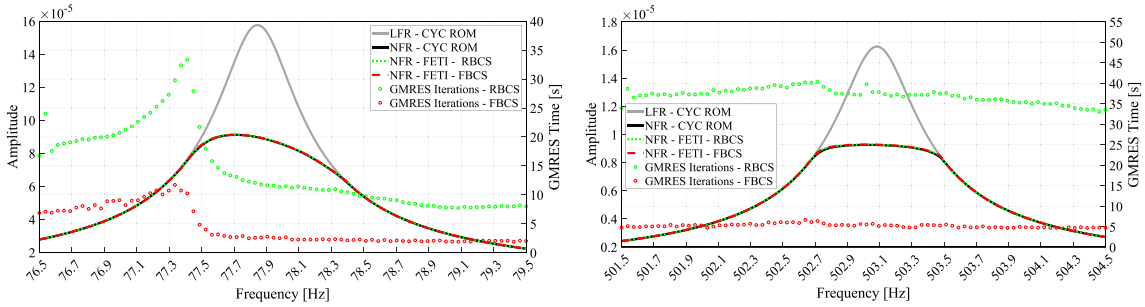


**Fig. 13.** GMRES times referred to nonlinear forced response between 76.5 Hz and 79.5 Hz (left) and between 501.5 Hz and 504.5 Hz (right).

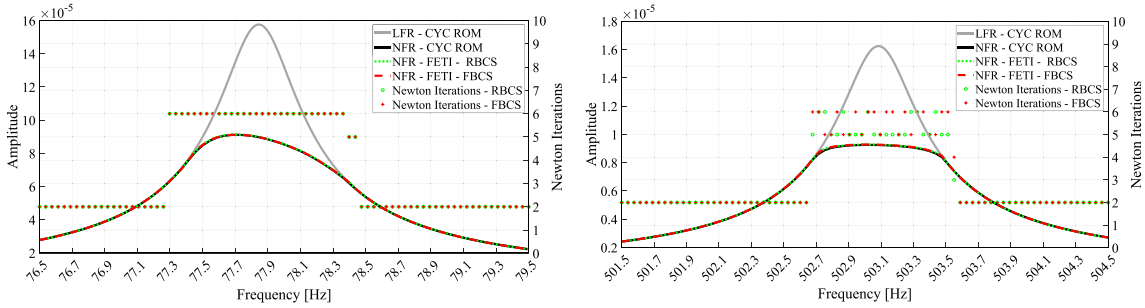


**Fig. 14.** NR iterations referred to nonlinear forced response between 76.5 Hz and 79.5 Hz (left) and between 501.5 Hz and 504.5 Hz (right).

between 501.5 Hz and 505.5 Hz it reduces the computational time of about the 55%. Even if the total size of the FBCS is higher than the RBCS (respectively an average of 12 and 40 deflated vectors per domain), this does not affect the total computational time and the time requested by the GMRES, as shown in Fig. 13.

## 5. Conclusions

The robustness and efficiency of domain decomposition methods, combined with the increasing computational power offered by modern HPC systems, are continuously pushing the limits of large-scale engineering simulations. This is particularly evident in structural dynamic analyses, where the size of FE models often constrains the applicability of state-of-the-art approaches. The FETI method provides a reliable and effective framework for the solution of nonlinear dynamic problems; however, for larger-scale linear systems, such as those arising from the introduction of Lagrange multipliers, computational costs can become significant.

Coarse spaces are introduced to deflate directions from the Krylov subspace that do not contribute to the solution. Identifying effective coarse spaces is challenging, and conventional approaches in structural dynamics have been shown to be inefficient in many cases. This work presents a novel Frequency Based Coarse Space (FBCS), specifically designed to address indefinite systems with a quadratic dependence on the scalar frequency parameter $\omega$, while preserving parallel scalability.

A weak scalability analysis demonstrates that the proposed FBCS maintains relatively high efficiency, mitigating the effects of domain decomposition and keeping the number of GMRES iterations approximately stable. The influence of the frequency parameter $\omega^2$ on GMRES convergence is assessed through a case study on a real FE model, confirming the improved robustness and efficiency of FBCS compared to the standard rigid body-mode coarse space (RBCS).

Validation on a full bladed-disk assembly confirms both the accuracy and effectiveness of the proposed methodology, showing that the introduction of the FBCS significantly reduces the number of GMRES iterations and the overall computational time (without increasing the NR iterations) thus providing a robust, efficient, and scalable solution that overcomes the limitations of RBCS and further extends the applicability of domain decomposition methods to large-scale structural dynamics simulations.

## CRediT authorship contribution statement

**Andrea Saponaro:** Writing – review & editing, Writing – original draft, Visualization, Validation, Software, Resources, Methodology, Investigation, Data curation, Conceptualization. **Giuseppe Battiato:** Writing – review & editing, Supervision, Resources, Methodology, Investigation, Conceptualization. **Christian Maria Firrone:** Writing – review & editing, Supervision, Resources, Methodology, Investigation, Conceptualization. **Stefano Zucca:** Writing – review & editing, Supervision, Resources, Methodology, Investigation, Funding acquisition, Conceptualization.

## Declaration of competing interest

The authors declare that they have no known competing financial interests or personal relationships that could have appeared to influence the work reported in this paper.

## Acknowledgments

This research is funded by the Ministry of University and Research (MUR), Italy as part of the HPC project which has received funding from the MUR on PNRR funding programme - Piano Nazionale di Ripresa e Resilienza, Mission 4 Component 2 Investment 1.4 with grant agreement no. CN00000013.

We acknowledge ISCRA for awarding this project access to the LEONARDO supercomputer, owned by the EuroHPC Joint Undertaking, and hosted by CINECA (Italy).

We would like to acknowledge Professor Claudio Canuto (Politecnico di Torino) and Professor Valeria Simoncini (Alma Mater Studiorum – Università di Bologna) for their valuable discussions and insightful suggestions.

## Data availability

The data presented in this study are available on reasonable request from the corresponding author.

## References


[1] Firrone CM, Zucca S. Modelling friction contacts in structural dynamics and its application to turbine bladed disks. Numer Anal-Theory Appl. 2011. pp. 301–34.
[2] Cardona A, Coune T, Lerusse A, Geradin M. A multiharmonic method for nonlinear vibration analysis. Int J Numer Methods Eng 1994;37(9):1593–608. https://doi.org/10.1002/nme.1620370911
[3] Craig Jr RR, Bampton MC. Coupling of substructures for dynamic analyses. AIAA J 1968;6(7):1313–9. https://doi.org/10.2514/3.4741
[4] Yang M-T, Griffin JH. A Reduced-Order model of mistuning using a subset of nominal system modes. J Eng Gas Turbines Power 1999;123(4):893–900. https://doi.org/10.1115/1.1385197
[5] Battiato G, Firrone CM. A modal based reduction technique for wide loose interfaces and application to a turbine stator. Mech Syst Signal Process 2020;139:106415. https://doi.org/10.1016/j.ymssp.2019.106415
[6] Bladh R, Castanier MP, Pierre C. Component-Mode-Based reduced order modeling techniques for mistuned bladed disks—Part I: theoretical Models. J Eng Gas Turb Power 2000;123(1):89–99. https://doi.org/10.1115/1.1338947
[7] Pourkiaee SM, Zucca S, Parker RG. Relative cyclic component mode synthesis: a reduced order modeling approach for mistuned bladed disks with friction interfaces. Mech Syst Signal Process 2022;163:108197. https://doi.org/10.1016/j.ymssp.2021.108197
[8] Battiato G, Firrone C. Reduced order modeling of large contact interfaces to calculate the non-linear response of frictionally damped structures. Procedia Struct Integr 2019;24:837–51.
[9] Battiato G, Firrone CM, Berruti TM, Epureanu BI, et al. A general method for sub-systems coupling for the dynamic analysis. In: International Conference on Noise and vibration Engineering and International Conference on uncertainty in structural dynamics (ISMA/USD), Leuven, Belgium; 2016.
[10] Toselli A, Widlund OB. Domain decomposition methods — algorithms and theory, vol. 34 of Springer Series in Computational Mathematics, Berlin, Heidelberg: Springer; 2005. https://doi.org/10.1007/b137868
[11] Farhat C, Roux F-X. A method of finite element tearing and interconnecting and its parallel solution algorithm. Int J Numer Methods Eng 1991;32:1205–27. https://doi.org/10.1002/nme.1620320604
[12] Farhat C, Lesoinne M, LeTallec P, Pierson K, Rixen D. FETI-DP: a dual–primal unified FETI method—Part I: A Faster Alternative to the Two-levelFETI method. Int J Numer Methods Eng 2001;50(7):1523–44. https://doi.org/10.1002/nme.76
[13] Paraschos GN, Vouvakis MN. The dual, overlapping primal FETI (FETI-DOP) domain decomposition. In: 2011 IEEE International Symposium on Antennas and Propagation (APSURSI); 2011. p. 2983–6, ISSN: 1947-1491. https://doi.org/10.1109/APS.2011.5997156.
[14] Dostál Z, Horák D, Kučera R. Total FETI—an easier implementable variant of the FETI method for numerical solution of elliptic PDE. Commun Numer Methods Eng 2006;22(12):1155–62. https://doi.org/10.1002/cnm.881
[15] Dostál Z, Kozubek T, Vondrák V, Brzobohatỳ T, Markopoulos A. Scalable TFETI algorithm for the solution of multibody contact problems of elasticity. Int J Numer Methods Eng 2010;82(11):1384–405.
[16] Gosselet P, Rixen D, Roux F-X, Spillane N. Simultaneous FETI and block FETI: robust domain decomposition with multiple search directions. Int J Numer Methods Eng 2015;104(10):905–27. https://doi.org/10.1002/nme.4946
[17] Farhat C, Avery P, Tezaur R, Li J. FETI-DPH: a dual-primal domain decomposition method for acoustic scattering. J Comput Acoust 2005;13(3):499–524. https://doi.org/10.1142/S0218396X05002761
[18] Farhat C, Chen P-S, Mandel J. A scalable Lagrange multiplier based domain decomposition method for time-dependent problems. Int J Numer Methods Eng 1995;38(22):3831–53. https://doi.org/10.1002/nme.1620382207
[19] Dostál Z, Gomes Neto FAM, Santos SA. Solution of contact problems by FETI domain decomposition with natural coarse space projections. Comput Methods Appl Mech Eng 2000;190(13):1611–27. https://doi.org/10.1016/S0045-7825(00)00180-8
[20] Blahoš J. Parallel harmonic balance method for analysis of nonlinear mechanical systems, [Ph.D. thesis], Diss. PhD Thesis. Imperial College London; 2022.
[21] Farhat C, Pierson K, Lesoinne M. The second generation FETI methods and their application to the parallel solution of large-scale linear and geometrically non-linear structural analysis problems. Comput Methods Appl Mech Eng 2000;184(2–4):333–74.
[22] Saponaro A, Battiato G, Firrone CM, Zucca S. Parallel computation of the nonlinear forced response of a bladed disk with friction contacts using the FETI method. J. Eng. Gas Turbines Power 2026;148(1):011021. https://doi.org/10.1115/1.4069613
[23] Rixen DJ, Farhat C. A simple and efficient extension of a class of substructure based preconditioners to heterogeneous structural mechanics problems. Int J Numer Methods Eng 1999;44(4):489–516. https://doi.org/10.1002/(SICI)1097-0207(19990210)44:4<489::AID-NME514>3.0.CO;2-Z
[24] Klawonn A, Rheinbach O. Deflation, projector preconditioning, and balancing in iterative substructuring methods: connections and new results. SIAM J Sci Comput 2012;34(1):459–84. https://doi.org/10.1137/100811118
[25] Spillane N, Rixen D. Automatic spectral coarse spaces for robust finite element tearing and interconnecting and balanced domain decomposition algorithms. Int J Numer Methods Eng 2013;95(11):953–90. https://doi.org/10.1002/nme.4534
[26] Saad Y, Schultz MH. Gmres: a generalized minimal residual algorithm for solving nonsymmetric linear systems. 1986.
[27] Klawonn A, Radtke P, Rheinbach O. FETI-DP methods with an adaptive coarse space. SIAM J Numer Anal 2015;53(1):297–320. https://doi.org/10.1137/130939675
[28] Leistner MC, Gosselet P, Rixen DJ. Recycling of solution spaces in multipreconditioned FETI methods applied to structural dynamics. Int J Numer Methods Eng 2018;116(2):141–60. https://doi.org/10.1002/nme.5918
[29] Armijo L. Minimization of functions having Lipschitz continuous first partial derivatives. Pac J Math 1966;16(1):1–3.
[30] Karypis G, Kumar V. METIS: a software package for partitioning unstructured graphs, partitioning meshes, and computing fill-reducing orderings of sparse matrices. 1997.
[31] Guennebaud G, Jacob B, et al. Eigen v3; 2010. http://eigen.tuxfamily.org.
[32] Balay S, Gropp WD, McInnes LC, Smith BF. Efficient management of parallelism in Object-Oriented numerical software libraries. In Arge E, Bruaset AM, Langtangen HP, editors. Modern software tools for scientific computing. Boston, MA: Birkhäuser; 1997. pp. 163–202. https://doi.org/10.1007/978-1-4612-1986-6_8
[33] Cameron TM, Griffin JH. An alternating frequency/time domain method for calculating the Steady-State response of nonlinear dynamic systems. J Appl Mech 1989;56(1):149–54. https://doi.org/10.1115/1.3176036
[34] Afzal M, Arteaga IL, Kari L. An analytical calculation of the jacobian matrix for 3d friction contact model applied to turbine blade shroud contact. Comput Struct 2016;177:204–17.
[35] Turisini M, Amati G, Cestari M. Leonardo: A pan-european pre-exascale supercomputer for hpc and ai applications. [arXiv preprint] arXiv:2307.16885. 2023.
[36] Gustafson JL. Reevaluating amdahl's law. Commun ACM 1988;31(5):532–3.